Version of Record: https://link.aps.org/doi/10.1103/kq2k-5dfg
Physical Review B, **114**, 144402 (2026). DOI: 10.1103/kq2k-5dfg

Interplay of Heisenberg frustration and anisotropic exchange in the magnetoelectric coupling of Janus CrIX (X = Cl, Br) monolayers

Hanif Yuandi Widyandaru* and Yoshihiro Gohda†
Department of Materials Science and Engineering, Institute of Science Tokyo, Yokohama 226-8501, Japan
(Dated: September 7, 2026)

Two-dimensional (2D) spintronics has emerged as a rapidly growing field due to its potential for precise manipulation of electron spins in nanoscale devices. In this work, we investigate the magnetic properties of Janus CrIX (X = Cl, Br) monolayers using first-principles calculations and atomistic spin simulations. Our study reveals that the magnetic ground state of CrIX is a helical spin spiral driven by intrachain isotropic Heisenberg frustration. Crucially, the broken inversion symmetry of the Janus structure induces a non negligible in-plane Dzyaloshinskii-Moriya interaction (DMI) while the low-symmetry spin-orbit-coupled environment also gives rise to substantial symmetric anisotropic exchange, which modulate the helical spin texture with a tilted spiral plane. By applying an external electric field, we demonstrate the ability to modulate these magnetic interactions through the interplay with the built-in electric field, resulting in a tunable deviation of the spin-spiral plane angle and wavelength. This direct correlation between the electric field and magnetic order highlights the magnetoelectric coupling in CrIX, establishing Janus CrIX as a model 2D platform for studying electrically tunable noncollinear magnetism.

I. INTRODUCTION

Recently, there has been great interest in multiferroic materials that exhibit the magnetoelectric effect [1], primarily driven by the potential to fine-tune magnetic properties via an external electric field [2, 3]. Among these, van der Waals (vdW) two dimensional (2D) materials possessing multiferroic orders have attracted significant attention [4]. While type-2 multiferroics are rarer than type-1, their intrinsic ferroic origins promise significantly stronger magnetoelectric coupling. These systems offer unique opportunities to explore novel coupling mechanisms in the 2D limit and enable the development of 2D-material-based nano spintronics [5].

The 2D magnetic semiconductor CrI_2 has emerged as a particularly promising candidate due to its tunable magnetic properties and a variety of exotic phases, including helimagnetism [6], multiferroicity [7], and strong Heisenberg-lattice coupling [8]. Although monolayer CrI_2 structurally preserves inversion symmetry, the Dzyaloshinskii-Moriya interaction (DMI) can emerge when this symmetry is broken through external means [9, 10]. For instance, in bilayer CrI_2, DMI becomes accessible by breaking inversion symmetry through specific stacking patterns [11–13]. Recent reports also suggest that multiferroicity in CrI_2 can arise from magnetic frustration, which couples spin chirality with electric polarization via generalized spin currents, potentially allowing for the control of magnetic properties through layer sliding [7]. However, DMI induced by specific stacking remains inherently weak. Furthermore, fine-tuning via interlayer sliding remains difficult from a practical device-application perspective [14].

To overcome these limitations, we propose CrIX as a Janus structure [15], wherein one side of the monolayer is chemically modified by replacing one set of halogen atoms with a different species such as Cl or Br. This structural asymmetry intrinsically breaks inversion symmetry and can significantly enhance spin-orbit-driven interactions. From a fabrication perspective, the advancement of synthesis techniques allows us to fabricate Janus structures [16, 17]. In addition, recent synthesis of bulk CrIBr [18] motivates the exploration of Janus CrIX (X = Cl, Br) monolayers as potential hosts for the emergence of multiferroic properties.

While prior theoretical studies suggested CrIBr and CrICl might support skyrmionic or bimeronic spin textures [19], those works neglected the Jahn-Teller (JT) distortion, which is well-established in the parent CrI_2 system [7, 20, 21]. This structural assumption fundamentally limits the allowed magnetic interactions, artificially suppressing the full anisotropic exchange matrix, including the asymmetric DMI and symmetric anisotropic exchange, that we identify are essential for a low-symmetry system such as JT-distorted Janus monolayers. Furthermore, the role of the symmetric anisotropic exchange could be non-negligible and needs to be examined in the context of Cr–I interaction [22, 23]. Additionally, since the Mermin-Wagner theorem prohibits long-range order in purely isotropic 2D systems [24], evaluating the single-ion anisotropy (SIA) is essential to understanding the magnetic stability of Janus CrIX.

In this work, we conduct systematic first-principles calculations to investigate the magnetic interactions in Janus CrIX (X = Cl, Br) monolayers. We analyze the Heisenberg exchange, anisotropic exchange, and SIA, demonstrating that CrIX possesses a spin-spiral ground state originating from Heisenberg frustration. The broken crystal symmetry leads to a substantial enhancement of the anisotropy-to-exchange ratio, with the spin spiral

* widyandaru.h.b68e@m.isct.ac.jp
† gohda@mct.isct.ac.jp

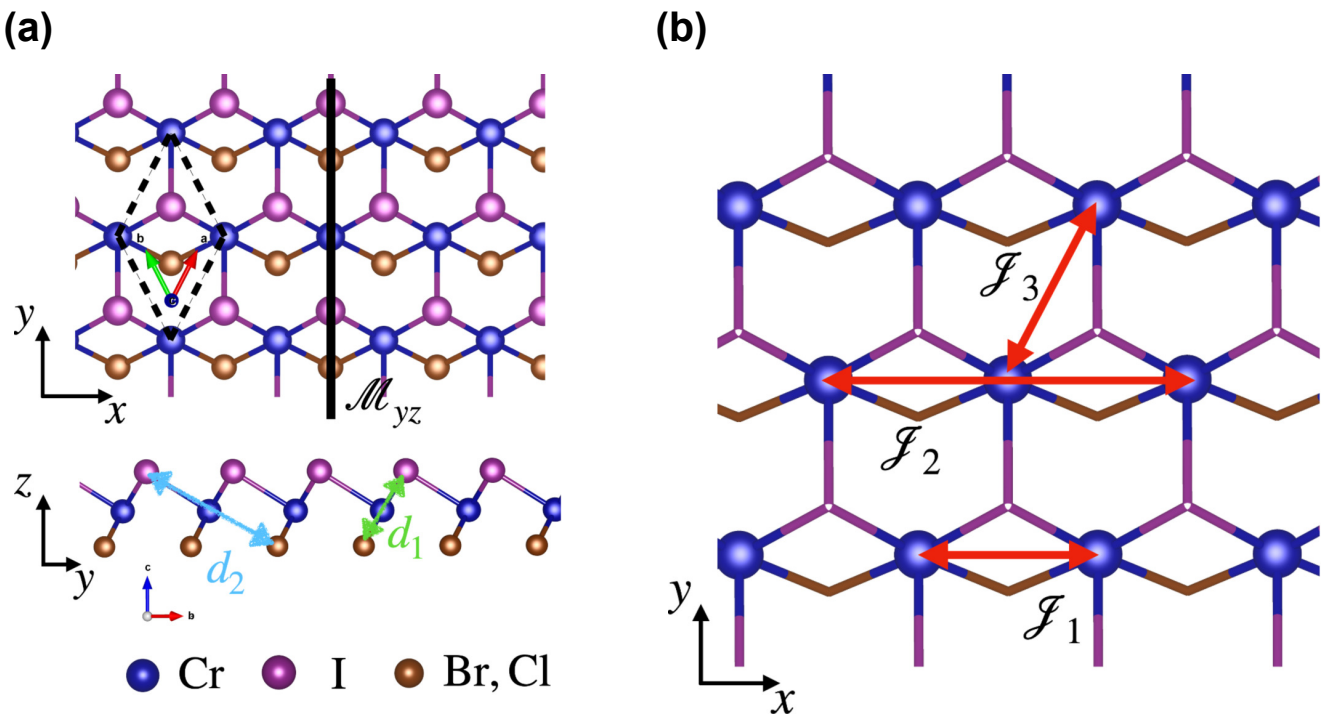

FIG. 1. (a) Top and side view of Janus CrIX with general Cartesian coordinates. The dashed black line indicates a unit cell. The $\mathcal{M}_{yz}$ mirror plane is indicated by a bold black line. The structure exhibits JT-distortion, showing the short (d_1) and long (d_2) I–Cr–X bonds that quantify the degree of structural asymmetry. The d_2 bond is parallel to the mirror plane $\mathcal{M}_{yz}$. (b) The schematic of magnetic interaction of CrIX. The red double headed-arrows indicate magnetic coupling $\mathcal{J}$ that consists of the isotropic Heisenberg interactions J, DMI $\boldsymbol{D}$, and symmetric anisotropic interactions $\boldsymbol{K}$.

resulting from the superposition of isotropic Heisenberg frustration and DMI. Furthermore, we show that an external electric field provides dual magnetoelectric control over the spin spiral: the inclination angle θ is governed by the modulation of anisotropic coupling, while an asymmetric field response of the isotropic Heisenberg exchanges independently tunes the Heisenberg frustration ratio, shifting the spin-spiral wavelength λ. Our findings establish Janus CrIX monolayers as promising platforms for 2D magnetoelectric materials and highlight a viable route toward understanding electric-field control of frustration-driven chiral magnetism in low-dimensional systems.

II. COMPUTATIONAL METHODS

We perform first-principles calculations of CrIX using density functional theory (DFT) with the projector augmented-wave (PAW) method [25] and the Perdew-Burke-Ernzerhof (PBE) exchange-correlation functional [26], as implemented in the VASP code [27]. A vacuum of approximately 15 Å is used to prevent interlayer interactions. A 450-eV plane-wave cutoff energy and a 0.06π-Å^{-1} k-mesh are used for the calculations. Lattice and atomic positions were relaxed until the forces acting on each atom are less than 0.01 eV/Å. Although van der Waals corrections are not strictly necessary for an isolated monolayer, the DFT-D3 functional by Grimme [28] was employed to derive the lattice constant from the bulk structure and retained in all subsequent electronic calculations to ensure consistency. We verified that the vdW correction does not affect the relative energy between the FM and AFM configurations. To properly describe the strongly correlated system, the DFT+U scheme with U = 5.0 eV is employed based on the Dudarev approach [29]. The U parameter is validated using the linear response method based on perturbation theory [30] within the supercell scheme (see Supplemental Material S1 [31]). For simulating the response to an electric field, an external electric field is applied along the z-axis by adding a sawtooth potential to the system. We note that while the upper limit of the applied electric field is 0.50 V/Å [32], these field values are employed theoretically to clearly elucidate the underlying mechanisms of the magnetoelectric coupling and to magnify the trends in the magnetic interactions.

To calculate the magnetic parameters, we employ the following spin Hamiltonian:

$$\mathcal{H} = \frac{1}{2}\sum_{n}\sum_{(i,j)_n} \hat{\mathbf{S}}_i \cdot \boldsymbol{\mathcal{J}}_{n,ij} \cdot \hat{\mathbf{S}}_j + \sum_i \hat{\mathbf{S}}_i \cdot \boldsymbol{\mathcal{A}}_{ii} \cdot \hat{\mathbf{S}}_i, \quad (1)$$

The first term describes the exchange coupling between pairs of spins (i, j) in the n-th neighbor shell. The second term represents the SIA of the Cr atom at each site i.

The full exchange matrix $\boldsymbol{\mathcal{J}}$ can be written as:

$$\boldsymbol{\mathcal{J}}_{ij} = \begin{pmatrix} J^{xx} & J^{xy} & J^{xz} \\ J^{yx} & J^{yy} & J^{yz} \\ J^{zx} & J^{zy} & J^{zz} \end{pmatrix} \tag{2}$$

Typically, this matrix can be decomposed as [33]:

$$\boldsymbol{\mathcal{J}}_{ij} = -J_{ij}\boldsymbol{I} + \boldsymbol{K}_{ij} + \boldsymbol{D}_{ij} \tag{3}$$

Here, the isotropic exchange scalar values are derived from the trace of the full exchange matrix, $J_{ij} = -\frac{1}{3}\mathrm{Tr}(\boldsymbol{\mathcal{J}}_{ij})$. The negative sign follows from our convention that $J > 0$ for FM and $J < 0$ for antiferromagnetic AFM. The second term is the symmetric anisotropic exchange interaction, comprising the Kitaev-like or two-ion anisotropy term $\boldsymbol{K}_{ij} = (\boldsymbol{\mathcal{J}}_{ij} + \boldsymbol{\mathcal{J}}_{ij}^{T})/2 + J_{ij}\boldsymbol{I}$ [34]. The last term is the DMI, which originates from the antisymmetric exchange interaction $\boldsymbol{D}_{ij} = (\boldsymbol{\mathcal{J}}_{ij} - \boldsymbol{\mathcal{J}}_{ij}^{T})/2$ and yields the three-dimensional 3D DMI vector [9, 10]. Furthermore, this model provides a more robust treatment of two-ion anisotropy than the typical approach $H_{ij}^{ani} = \sum_{ij} S_i^z S_j^z$ [35]. In general, the SIA can be represented as a matrix, analogous to the $\boldsymbol{\mathcal{J}}_{ij}$. In high-symmetry systems, it is common to assume that only the A^{zz} component (corresponding to uniaxial anisotropy along the z-axis) is significant, with all other elements vanishing due to rotational symmetry. However, since our system lacks rotational symmetry, the SIA matrix contains nonzero off-diagonal and additional diagonal elements, and thus cannot be simplified to only consider the A^{zz} term. Therefore, we analyze each element (both diagonal and off-diagonal) of the SIA matrix to obtain an accurate picture of the SIA. Since $S_i^2 = (S_i^x)^2 + (S_i^y)^2 + (S_i^z)^2$, we can express the diagonal part of the SIA matrix as [36]:

$$\begin{aligned} H_{\mathrm{SIA}}^{\mathrm{dia}} &= S^x A^{xx} S^x + S^y A^{yy} S^y + S^z A^{zz} S^z \\ &= A^{xx} S^2 + \big(A^{yy} - A^{xx}\big)(S^y)^2 \\ &\quad + \big(A^{zz} - A^{xx}\big)(S^z)^2 \end{aligned} \tag{4}$$

The $\boldsymbol{\mathcal{A}}_{ii}$ matrix can now be rewritten as:

$$\boldsymbol{\mathcal{A}}'_{ii} = \boldsymbol{\mathcal{A}}_{ii} - A^{xx}\mathbf{I} = \begin{pmatrix} 0 & A^{xy} & A^{xz} \\ A^{yx} & A^{yy} - A^{xx} & A^{yz} \\ A^{zx} & A^{zy} & A^{zz} - A^{xx} \end{pmatrix} \tag{5}$$

Both $\boldsymbol{\mathcal{J}}$ and $\mathbf{A}$ are 3×3 matrices, which capture the anisotropic nature of the interactions. The elements of these matrices can be extracted using the four-states method, which involves mapping the ab initio energies of specific spin configurations onto the considered Hamiltonian [37, 38].

Using the extracted magnetic parameters, atomistic spin simulations based on Monte Carlo (MC) were performed using the VAMPIRE package [39] to calculate the ground-state spin texture and the Néel temperature (T_N). An 81 nm × 81 nm slab model was used, with periodic boundary conditions applied in the in-plane directions. To determine the low-temperature spin texture, a randomly distributed spin configuration was used as the initial state and a zero-field-cooling procedure was adopted, in which the temperature was gradually decreased from 50 K to near 0 K following a Gaussian cooling schedule. A total of 3×10^6 calculation steps were performed, including 5×10^3 initial equilibration steps. To determine T_N, a separate temperature-dependent MC simulation was performed starting from the resulting low-temperature spin configuration and progressively increasing the temperature from 0 to 30 K in increments of 0.15 K. At each temperature, 2×10^3 MC steps were used for equilibration, followed by 5×10^5 MC steps for statistical averaging. The ordering temperature was identified as the temperature corresponding to the maximum of the specific heat C_v.

III. RESULTS AND DISCUSSION

Geometric and structural properties

Distinct from previous theoretical studies that assumed a highly symmetric C_{3v} ($P3m1$) structure for Janus Cr$I$$X$ monolayers [19], our analysis reveals that the ground state crystal structure is governed by a JT distortion as shown in Fig. 1(a), similar to the parent CrI_2 system [20, 40]. This electronic instability lifts the degeneracy of the Cr $3d$ orbitals, driving a structural transition to the lower-symmetry monoclinic C_s (Cm). The degree of bond asymmetry introduced by the JT distortion can be quantified by $\Delta\mathrm{JT} = d_2 - d_1$, where d_2 and d_1 are the longest and shortest I–Cr–X bond lengths along the intrachain direction, respectively. We find ΔJT(I–Cr–Cl) = 1.22 Å and ΔJT(I–Cr–Br) = 1.15 Å, indicating that CrICl exhibits greater structural asymmetry along the magnetic exchange path than CrIBr.

We confirm the stability of this distorted phase by calculating the total energy difference relative to the non distorted phase as shown in Fig. S2 [31], finding the Cm structure to be energetically favorable for both CrIBr and CrICl. Our calculated lattice constants are $a = 4.146$ Å and $a = 4.152$ Å for CrIBr and CrICl, respectively. The optimized lattice constant of CrIBr is in good agreement with experimental reports for bulk CrIBr [18]. The distorted phase has a quasi-one-dimensional 1D atomic chain-like structure along the x-axis.

The crucial consequence of this structural distortion is its impact on the magnetic interactions. Symmetry breaking inherent to the Cm space group dictates the allowed components of the magnetic exchange matrix, fundamentally enabling the specific DMI and symmetric anisotropic terms that we analyze in the following sections.

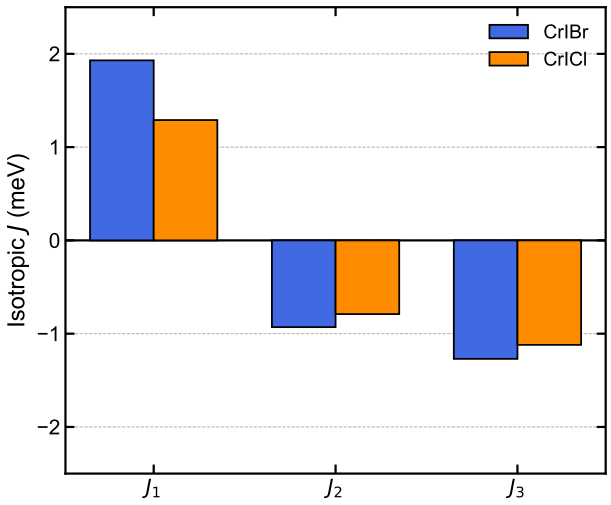

FIG. 2. Calculated isotropic Heisenberg exchange parameters (J_1, J_2, J_3) for CrIBr and CrICl. Note the ferromagnetic J_1 and antiferromagnetic J_2 and J_3 couplings, which lead to Heisenberg frustration.

Isotropic and anisotropic magnetic exchange interactions

We began by analyzing the isotropic exchange interactions for six unique nearest-neighbor pairs using the four-state method without spin-orbit coupling (SOC), as detailed in Supplementary Material, Fig. S3. [31] Our calculations reveal that further-neighbor pairs, particularly those not directly bridged by a ligand atom, exhibit negligible isotropic Heisenberg contributions. Consequently, in this study, we focus exclusively on the three strongest interactions: (i) the nearest intrachain pair ($\mathcal{J}_1$), (ii) the second nearest intrachain pair ($\mathcal{J}_2$), and (iii) the nearest interchain pair ($\mathcal{J}_3$) as shown in Fig. 1(b). Other couplings were found to be vanishingly weak and do not influence the ground state of magnetic order.

Due to the crystal structure, the components of the Hamiltonian will be constrained. We propose minimal model spin Hamiltonian:

$$\begin{aligned}\mathcal{H} =& \frac{1}{2}\sum_{n=1}^{3}\sum_{(i,j)_n}\Big[-J_n\hat{\mathbf{S}}_i\cdot\hat{\mathbf{S}}_j+\mathbf{D}_n\cdot(\hat{\mathbf{S}}_i\times\hat{\mathbf{S}}_j)\\ &+\hat{\mathbf{S}}_i\cdot\boldsymbol{K}_n\cdot\hat{\mathbf{S}}_j\Big]+\sum_i\hat{\mathbf{S}}_i\cdot\boldsymbol{\mathcal{A}}_{ii}\cdot\hat{\mathbf{S}}_i\end{aligned} \tag{6}$$

The sole mirror symmetry $\mathcal{M}_{yz}$ of the crystal structure imposes distinct constraints on the interaction matrices based on both the local site symmetry and the two-ion exchange geometry. For the SIA, mirror plane operation $(x \to -x)$ strictly forces the xy and xz off-diagonal elements of the SIA matrix $\boldsymbol{\mathcal{A}}_{ii}$ to zero.

For the two-ion exchange interactions, the antisymmetric exchange matrix $\boldsymbol{D}_n$ is expressed as the DMI vector $\mathbf{D}_n$ via $\hat{\mathbf{S}}_i\cdot\boldsymbol{D}_n\cdot\hat{\mathbf{S}}_j = \mathbf{D}_n\cdot(\hat{\mathbf{S}}_i\times\hat{\mathbf{S}}_j)$. Because of the intra-

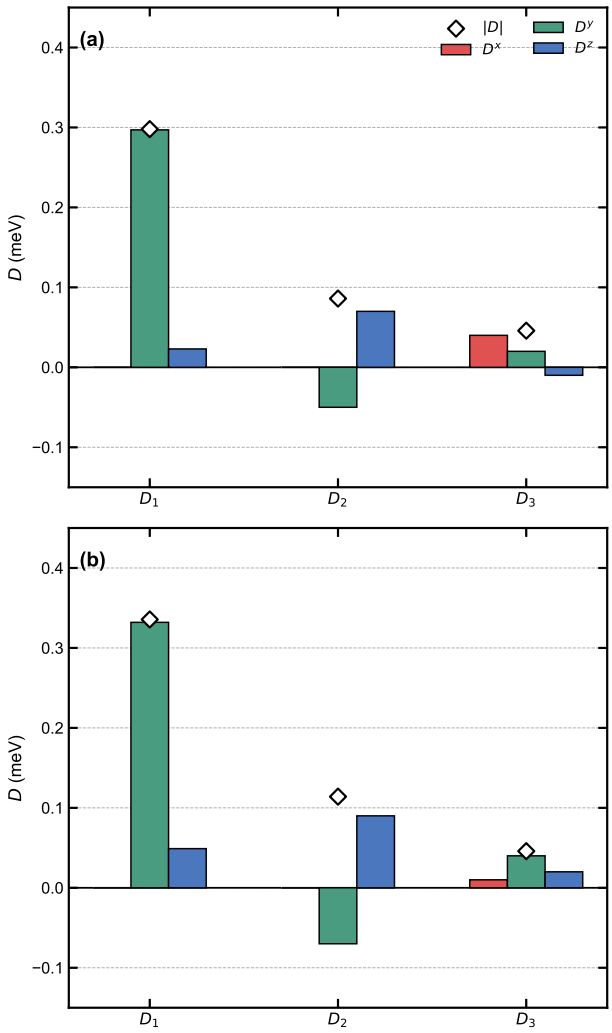

FIG. 3. Neighbor-resolved components and total magnitudes of DMI of (a) CrIBr and (b) CrICl, showing that the DMI vector orientation is strictly constrained by crystal symmetry.

chain bonds $(n = 1, 2)$ perpendicular to the $\mathcal{M}_{yz}$ plane, their interactions, parameterized by $(J_n, \mathbf{D}_n, \boldsymbol{K}_n)$, are subject to identical symmetry restrictions. Specifically, the reflection symmetry dictates that the xy and xz off-diagonal elements of the symmetric anisotropic exchange matrices $\boldsymbol{K}_1$ and $\boldsymbol{K}_2$ vanish. Furthermore, Moriya's rule [10] confines their DMI vectors to the mirror plane, strictly requiring $D_1^x = D_2^x = 0$.

In distinct contrast, the interchain bond $(n = 3)$ does not lie on $\mathcal{M}_{yz}$. As a result, its interaction parameters $(J_3, \mathbf{D}_3, \boldsymbol{K}_3)$ remain entirely unconstrained by this mirror operation, allowing for all three $\mathbf{D}_3$ spatial components and a fully populated $\boldsymbol{K}_3$ matrix. These symmetry-enforced constraints firmly establish the minimal spin Hamiltonian required to capture the system's essential physics, independent of the specific halogen substitution.

To provide a more accurate description of the magnetic interactions, we recalculated these parameters by

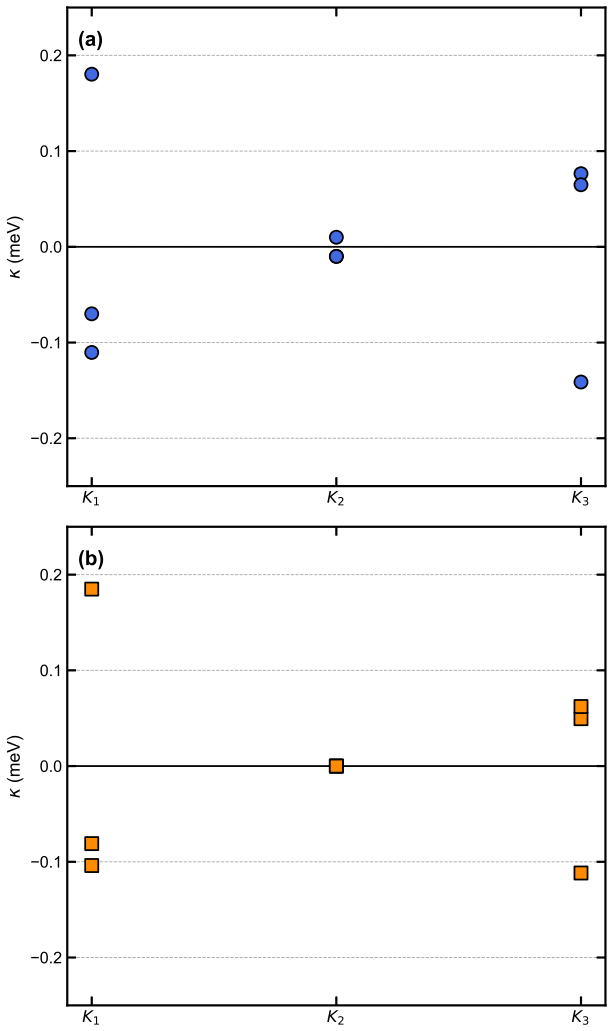

FIG. 4. Eigenvalues of the symmetric anisotropic exchange matrix of (a) CrIBr and (b) CrICl. One unique eigenvalue reflects two-ion uniaxial anisotropy for corresponding spin pair.

including SOC. As shown in Fig. 2, the isotropic coupling J_1 is FM, whereas J_2 and J_3 are AFM for both CrIBr and CrICl. The AFM nature of J_3 suggests an AFM stripe ground state in the collinear limit, similar to the magnetic structure of CrI_2 [8]. This AFM coupling arises because the direct interaction dominates over the competing FM superexchange for this pair. The FM superexchange pathway is suppressed by the local symmetry imposed by the JT distortion, which inhibits $d-p-d$ hopping. Crucially, the presence of the AFM J_2 interaction introduces Heisenberg frustration. The magnitude of the ratio between J_1 and J_2 satisfies the classical condition for a spiral helimagnetic order, $|J_1| < 4|J_2|$, which is in agreement with experimental observations of spiral order in CrIBr [18].

Due to the broken inversion symmetry inherent in the Janus structure, both CrIBr and CrICl exhibit significant DMI. This interaction arises from the antisymmetric components of the exchange matrix, $\mathcal{J}$. The DMI vector, D, is defined in terms of the matrix elements as $D^x = \frac{1}{2}(J^{yz} - J^{zy})$, $D^y = \frac{1}{2}(J^{zx} - J^{xz})$, and $D^z = \frac{1}{2}(J^{xy} - J^{yx})$. This DMI is expected to further stabilize the spin spiral state initially induced by Heisenberg frustration. Figures 3(a) and (b) display the component-resolved DMI vectors and their magnitudes for CrIBr and CrICl, respectively. The DMI of the nearest intrachain interaction D_1 exhibits a significant in-plane DMI component, while the second intrachain D_2 shows a mixture of out-of-plane and in-plane components. The interchain interaction D_3 makes the smallest contribution. It is important to note that the D^x components for D_1 and D_2 are exactly zero, consistent with the minimal symmetry constraint. The consistency of our results with these symmetry rules also serves as a strong validation of our DMI extraction method. We observe that the magnitude of the DMI decreases following the trend $|D_1| > |D_2| > |D_3|$. Furthermore, CrIX exhibits asymmetric DMI ($|D_1| \neq |D_3|$), a consequence of its crystal structure. This unique condition is predicted to enable stable spin-spiral switching driven by spin-orbit-torque [41].

The larger DMI magnitude in CrICl compared to CrIBr is a direct consequence of the greater bond asymmetry ΔJT(I–Cr–Cl) > ΔJT(I–Cr–Br) established in the structural analysis, which produces stronger local inversion symmetry breaking along the I–Cr–X exchange path, dominating over the heavier-ligand SOC advantage of Br. The robustness of the DMI is highlighted by the ratio of the DMI magnitude to the isotropic Heisenberg exchange, $|D/J|$ [42]. For the first nearest neighbor, we find $|D/J|$ values of approximately 0.15 for CrIBr and 0.26 for CrICl. This ratio provides a quantitative estimate of the DMI's ability to perturb the collinear Heisenberg order; for instance, a $|D/J|$ value exceeding 0.1 is typically considered sufficient to introduce spin canting and stabilize spin spiral formation [43, 44]. Notably, the $|D/J|$ ratios obtained here are 0.15 for CrIBr and 0.26 for CrICl, which are among the largest reported in 2D Janus magnets, comparable to the large $|D/J|$ predicted in Janus MnSTe (0.25) [43], and significantly exceeding those of Janus CrXTe (0.02–0.14) [45], Janus Ni-halide (0.04–0.10) [46], Janus V-halide (0.04–0.15) [47], and stacking-induced DMI in bilayer CrI_2 ($\sim 10^{-3}$) [11] (see Table S1 in Supplemental Material [31]). The microscopic origin of this enhancement is different from that in bilayer CrI_2. In the bilayer system, inversion symmetry is broken by the stacking or relative sliding of two otherwise centrosymmetric layers, and the resulting DMI is associated primarily with comparatively weak interlayer exchange paths. In Janus CrIX, by contrast, inversion symmetry is broken intrinsically within each monolayer by the inequivalence of the two halogen species. The resulting local bond asymmetry directly affects the dominant exchange paths, leading to much stronger DMI.

The SIA matrix elements for the Cr ion in CrIBr and CrICl, derived from our *ab initio* energy mapping, are

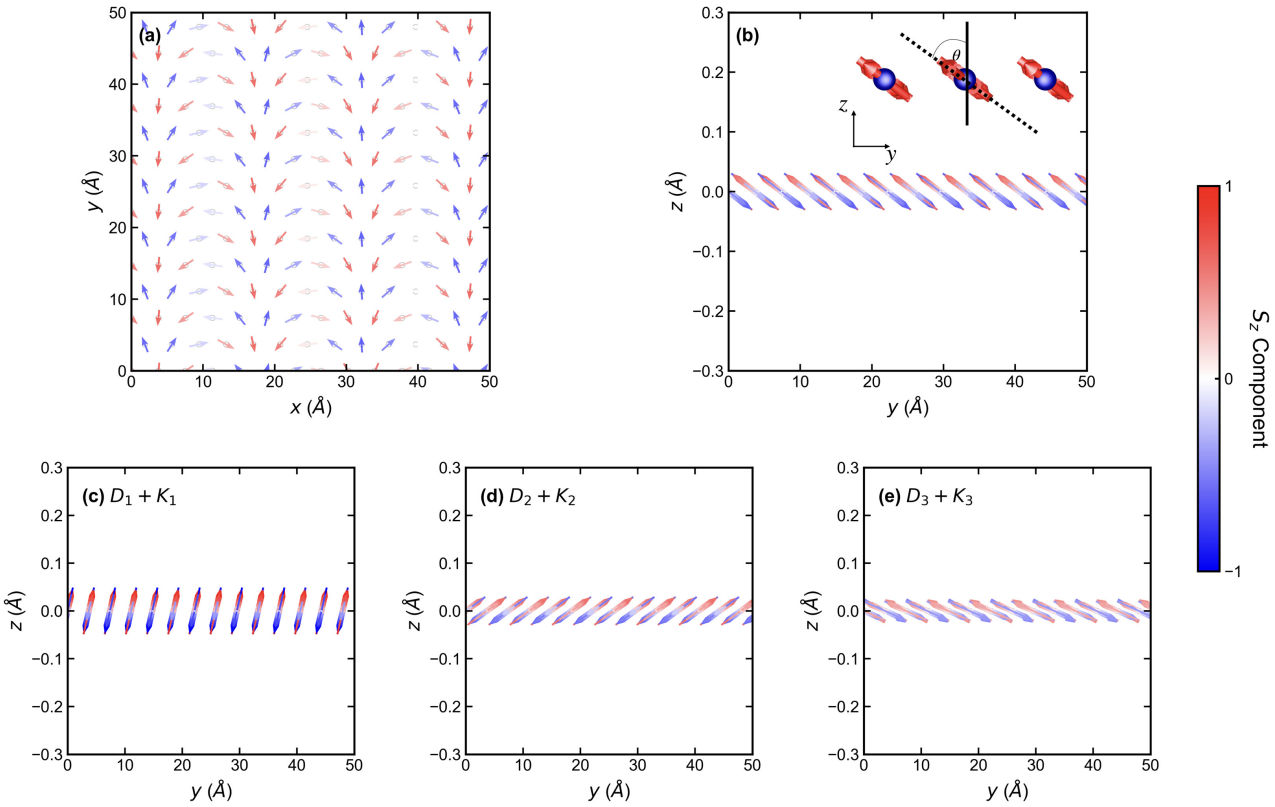

FIG. 5. Ground state spin textures in Janus CrIBr monolayers. (a) Top view (xy-plane) and (b) side view (yz-plane) of the ground state helical spin spiral stabilized by the full Hamiltonian, including isotropic Heisenberg exchange (J), DMI, symmetric anisotropic exchange (K), and SIA (A). The color gradient represents the out-of-plane spin component (S_z). Angle θ is defined as the inclination of the spin-spiral plane. (c)-(e) Neighbor-resolved contributions to the spin texture viewed in the yz-plane, isolating the effects of the first (D_1+K_1), second (D_2+K_2), and third (D_3+K_3) neighbor anisotropic interactions, respectively. The pronounced tilting of the spiral plane is primarily driven by the anisotropic interaction.

TABLE I. Calculated SIA matrix elements (in meV) for the Cr site in CrIBr and CrICl. A'_{ii} is defined as the difference between the maximum and minimum eigenvalues of the SIA matrix.

Material	A^{xy}	A^{xz}	A^{zy}	$A^{zz}-A^{xx}$	$A^{yy}-A^{xx}$	A'_{SIA}
CrIBr	0.00	0.00	0.07	-0.08	-0.18	0.21
CrICl	0.00	0.00	0.11	-0.07	-0.25	0.31

presented in Table I. Note that the SIA satisfies these relations: $A^{xy} = A^{yx}$, $A^{xz} = A^{zx}$, and $A^{zy} = A^{yz}$. For CrIBr, we find the diagonal anisotropy components relative to the x-axis to be $A^{zz} - A^{xx} = -0.08$ meV and $A^{yy} - A^{xx} = -0.18$ meV. Upon substituting Br with the more electronegative Cl, the magnitude of the $A^{yy} - A^{xx}$ becomes more negative to -0.25 meV, while the $A^{zz} - A^{xx}$ becomes slightly less negative to -0.07 meV. The calculated non-zero off-diagonal A^{zy} term is present in both compounds, with values of 0.07 meV for CrIBr and 0.11 meV for CrICl. The A^{xy} and A^{xz} components are zero, consistent with the $\mathcal{M}_{yz}$ symmetry. In contrast, the presence of A^{zy} indicates mixing between the z and y components, resulting in the magnetic easy axis being tilted within the y-z plane. By calculating the eigenvector corresponding to the lowest eigenvalue of the $\boldsymbol{\mathcal{A}}'_{ii}$ matrix, we find that the easy axis of the SIA is parallel to the elongated bond d_2 of I–Cr–X [see Fig. 1(a)], while the hard axis is along x. Thus, the preferred SIA direction is attributed to the Jahn-Teller distortion [48], which strengthens the anisotropy along the elongation axis. To quantify the scalar strength of the SIA, we define the anisotropy coupling as $A'_{SIA} = \varepsilon_{\max} - \varepsilon_{\min}$, where ε represents the eigenvalues of the matrix $\boldsymbol{\mathcal{A}}'_{ii}$.

We next address the symmetric anisotropic exchange, represented by the traceless symmetric matrix $\boldsymbol{K}_{ij}$, as shown in Table II. Since the $\boldsymbol{K}_{ij}$ matrix contains both two-ion anisotropy and the Kitaev term, the preferred anisotropy direction depends on the relative alignment of the spins. When spins $\hat{\mathbf{S}}_i$ and $\hat{\mathbf{S}}_j$ are parallel, the term $\hat{\mathbf{S}}_i^T \boldsymbol{K}_{ij} \hat{\mathbf{S}}_j$ behaves analogously to SIA ($\hat{\mathbf{S}}_i^T \boldsymbol{\mathcal{A}}_{ii} \hat{\mathbf{S}}_i$), favoring the direction corresponding to the lowest eigenvalue of $\boldsymbol{K}_{ij}$. Conversely, when spins are antiparallel, the interaction favors the direction of the highest eigenvalue [33]. Using the same procedure as for calculating the SIA, the eigenvalues of this matrix are plotted

in Fig. 4. We denote these eigenvalues as κ_α, κ_β, and κ_γ, which encompass the combined effects of two-ion anisotropy and the Kitaev term [49]. We identify κ_γ as the unique eigenvalue corresponding to the bond direction, while $\kappa_\alpha \approx \kappa_\beta$. The negligible difference between κ_α and κ_β indicates isotropic plane governed by corresponding eigenvectors. Consequently, we define the effective symmetric anisotropic contribution as $K = \kappa_\gamma - \bar{\kappa}$, where $\bar{\kappa} = (\kappa_\alpha + \kappa_\beta)/2$.

TABLE II. Calculated symmetric anisotropic matrix elements (in meV) for the Cr–Cr exchange pair in CrIBr and CrICl.

Material		K^{xx}	K^{yy}	K^{zz}	K^{xy}	K^{xz}	K^{yz}	$K = \kappa_\gamma - \bar{\kappa}$
CrIBr	$\boldsymbol{K}_1$	-0.07	0.10	-0.03	0.00	0.00	-0.13	0.27
	$\boldsymbol{K}_2$	-0.01	0.00	0.00	0.00	0.00	-0.01	0.01
	$\boldsymbol{K}_3$	-0.02	0.05	-0.03	0.05	0.09	-0.05	-0.21
CrICl	$\boldsymbol{K}_1$	-0.08	0.09	-0.01	0.00	0.00	-0.14	0.28
	$\boldsymbol{K}_2$	0.00	0.00	0.00	0.00	0.00	0.00	0.00
	$\boldsymbol{K}_3$	-0.01	0.04	-0.03	0.04	0.07	-0.04	-0.17

Our analysis reveals significant symmetric anisotropic exchange for the Janus Cr$I$$X$ monolayers. We find substantial values for the first intrachain neighbor K_1 (0.27 meV for CrIBr; 0.28 meV for CrICl) and the interchain neighbor K_3 (-0.21 meV for CrIBr; -0.17 meV for CrICl), whereas the second intrachain neighbor term K_2 is remarkably small (about 0.01 meV). The opposite signs of K_1 and K_3 should be interpreted together with the corresponding magnetic correlations. The sign difference reflects the bond-dependent nature of the symmetric anisotropic exchange. For the FM J_1 interaction, neighboring spins tend to align parallel, such that the symmetric anisotropic exchange favors the eigenvector associated with the lowest eigenvalue. Since $K_1 = \kappa_\gamma - \bar{\kappa} > 0$, the κ_α and κ_β eigenvalues lie below κ_γ, and the preferred spin orientation is therefore associated with the corresponding α–β subspace. In contrast, J_3 is AFM, for which antiparallel spin alignment reverses the energetic preference and favors the largest eigenvalue. Since $K_3 < 0$, κ_α and κ_β lie above κ_γ. Therefore, despite the opposite signs of K_1 and K_3, their anisotropic contributions can favor similar spin-orientation tendencies because they act on FM- and AFM-correlated bonds, respectively. This behavior is consistent with the magnetic-order-dependent character of Kitaev-like anisotropy [50].

Furthermore, the magnitude of K_1 is comparable to the DMI D_1, with $|K_1|/|D_1|$ ratios of approximately 0.9 for CrIBr and 0.6 for CrICl. This indicates that the symmetric anisotropic exchange is a significant factor in determining the magnetic ground state and cannot be neglected in favor of DMI alone. The strong contribution from symmetric anisotropic exchange is likely due to significant Kitaev coupling, similar to the case of NiI_2 [33, 51].

Spin texture and thermal stability

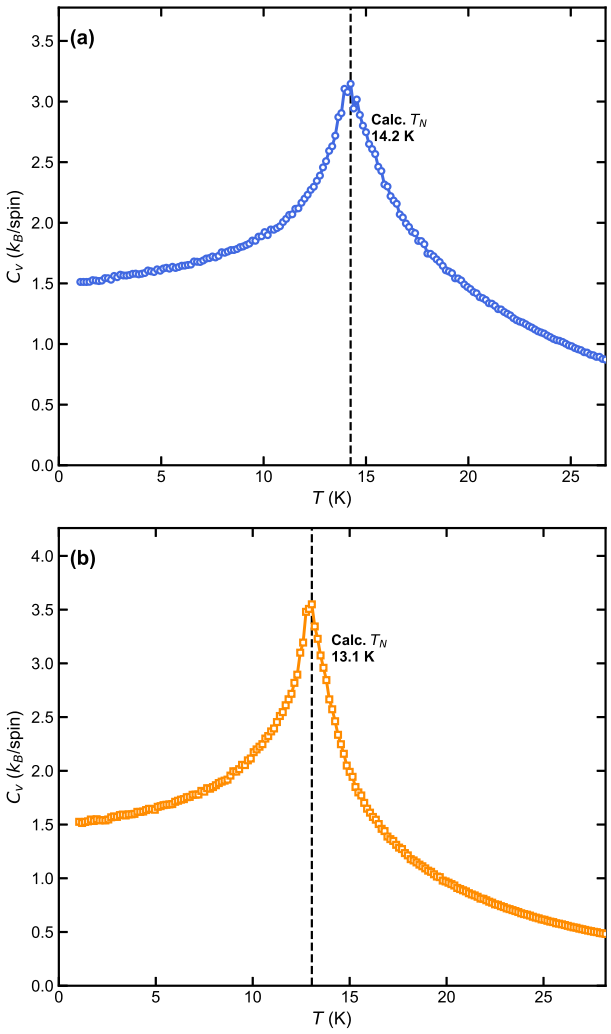

FIG. 6. The MC calculated specific heat as a function of temperature for Janus monolayers of (a) CrIBr and (b) CrICl.

Using the calculated magnetic coupling parameters, we determine the magnetic ground state of the Janus monolayers via atomistic spin simulations. Figures 5(a), 5(b), and S4 [31] show the spin texture of CrIBr and CrICl. The ground state is identified as an antiferromagnetic helical spiral. This helical spin originates primarily from Heisenberg frustration, specifically the $J_1 - J_2$ competition, rather than DMI-induced spin canting, as indicated by the ratio $|J_2/J_1| > |D_1/J_1|$. The spin textures resulting from pure Heisenberg frustration and combined Heisenberg-DMI frustration are compared in Fig. S5 [31].

The coplanar helical ground state of CrIBr is characterized by a propagation vector $q = (0.216, 0, 0)$ Å^{-1} ($q = (0.285, 0, 0)$ Å^{-1} for CrICl). It should be noted that the periodic boundary conditions of the finite Monte Carlo simulation cell mathematically enforce a quantized q-vector, approximating the intrinsic period driven by the

isotropic $J_1 - J_2$ frustration. We validate that the overall magnetic trends are robust against this finite-size quantization, as confirmed by the cell-size convergence shown in the Supplemental Material Fig. S9 [31]. The spin spiral propagates along the intrachain direction, similar to the reported observation in bulk CrIBr [18]. Interestingly, the spin spiral in CrIBr does not lie flat but stabilizes in a tilted plane θ as shown in Fig. 5(b), a feature similar to that reported in materials with strong anisotropic exchange [46, 52].

To elucidate the microscopic origin of this tilting, we analyze the neighbor-resolved anisotropic contributions to the spin texture [Figs. 5(c) to 5(e)]. When considering the isotropic Heisenberg interaction alongside specific anisotropic terms, we observe distinct behaviors: the strong in-plane DMI D_1 favors an out-of-plane spiral rotation [Fig. 5(c)], whereas the second-neighbor interaction $D_2 + K_2$ introduces a complex mixing between out-of-plane and in-plane components (Fig. 5(d)). Finally, the third-neighbor interaction is dominated by the symmetric anisotropic term K_3, further stabilizing the tilted plane [Fig. 5(e)].

With the ground-state magnetic texture established, we evaluate the thermal stability of the helical phase by calculating the specific heat capacity C_v as a function of temperature using MC simulations. As shown in Fig. 6, the C_v exhibits a pronounced peak at $T_N \approx 14.2$ K for CrIBr (13.1 K for CrICl), corresponding to the T_N of the phase transition from the helical spiral to the paramagnetic state. Our predicted T_N is slightly higher than the experimental value of ~ 12 K reported for bulk CrIBr [18].

We note that this comparison between the monolayer T_N and the bulk experimental value is justified because bulk CrIBr is a layered van der Waals material with weak interlayer magnetic coupling, meaning the ordering temperature is predominantly governed by the in-plane exchange interactions. This small overestimation is expected, as our classical spin model neglects quantum fluctuations, which are known to suppress the ordering temperature in low-dimensional magnetic systems [53, 54]. Additionally, the simulation assumes a pristine crystal lattice, whereas experimental values are inevitably reduced by structural defects [55]. Considering these factors, the close agreement between our theoretical prediction and the experimental result validates the accuracy of the calculated exchange parameters.

Magnetoelectric effect

Since the anisotropic coupling is a relativistic effect driven by spin-orbit coupling, an external electric field can effectively modulate the magnetic exchange parameters, thereby tuning the spin spiral. Given the similar trends in magnetic coupling between CrIBr and CrICl, we focus on CrIBr as the representative system. Figure 7(a) illustrates the evolution of the magnetic coupling coefficients in CrIBr under a perpendicular electric field E_z.

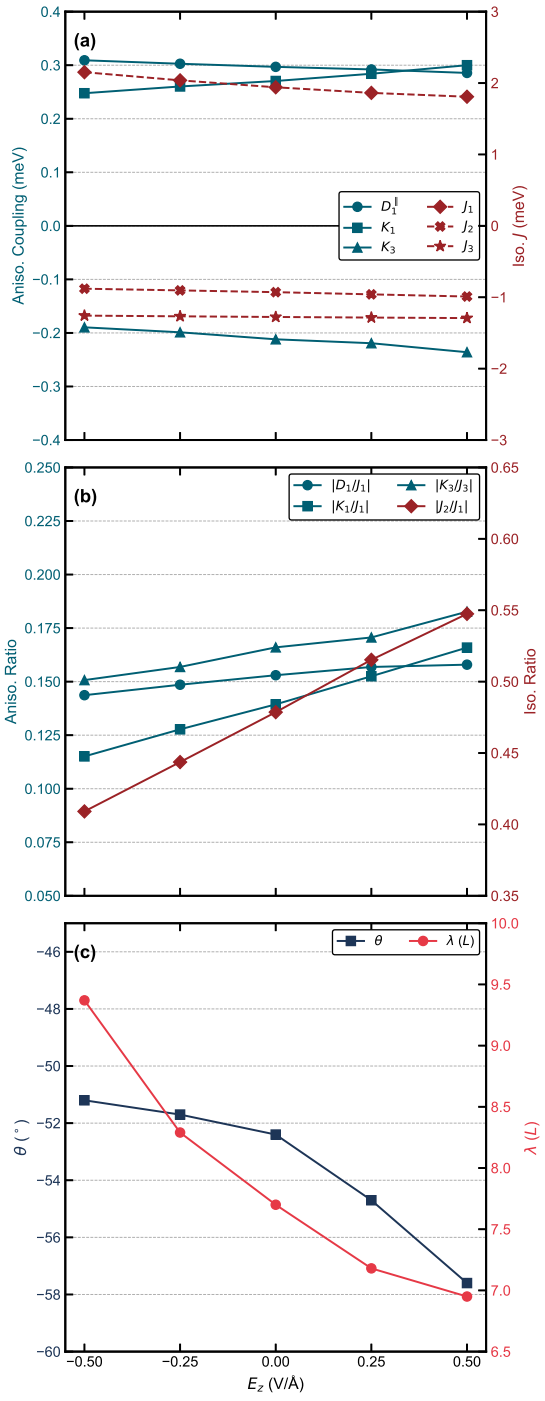

FIG. 7. Electric-field control of magnetic interactions and spin texture. (a) Variation of the anisotropic $(D_1^{\parallel}, K_1, K_3)$ and isotropic (J_1, J_2, J_3) exchange coupling coefficients as a function of the external electric field E_z. (b) Dependence of the anisotropy-to-isotropic interaction ratios $(|D_1^{\parallel}/J_1|, |K_1/J_1|, |K_3/J_3|)$ and isotropic ratio $|J_2/J_1|$. (c) The plot of inclination angle θ (in degrees) and wavelength λ (in Cr-Cr intrachain distance $L = 0.378$ nm), demonstrates dual control of the spin spiral.

This high field regime is primarily of theoretical interest to establish the physical trend and the continuous modulation of the anisotropic coupling. We neglect the effects of D_2, D_3, and K_2, as they are insignificant compared to the other anisotropic couplings. The nearest-neighbor isotropic exchange J_1 is robustly modified by the electric field, changing significantly more than J_2 and J_3 because it relies heavily on the superexchange mechanism mediated by ligand bonding orbitals, where the hopping interaction is strongly perturbed by the external field. This is similar to the behavior observed in VI_2 [56]. Additionally, the in-plane DMI component decreases slightly as the field increases due to the external field opposing the intrinsic Janus polarization. The symmetric anisotropic terms K_1 and K_3 also show clear modulation. In this case, under an electric field, the DMI D and symmetric anisotropy K exhibit opposite trends due to an interference effect [57]. Specifically, a negative electric field $E_z < 0$ promotes DMI at the direct expense of symmetric anisotropic coupling, indicating that these two interactions are coupled and cannot be independently maximized.

Figure 7(b) quantifies the modulation through the ratios of anisotropic to isotropic coupling. The Heisenberg frustration ratio $|J_2/J_1|$ is robustly modified by the electric field due to the imbalanced response between J_1 and J_2, and these ratios increase under positive electric field. The ratio of anisotropic coupling to isotropic also shows similar behavior, indicating the interplay between Heisenberg frustration and anisotropic interactions is continuously tuned by the electric field.

Figure 7(c) demonstrates dual control of the spin-spiral inclination angle θ and wavelength λ. Furthermore, we clarify the correlation between the anisotropy-to-isotropic interaction ratios and the inclination angle θ, indicating that θ is regulated by anisotropic coupling similar to the case of Janus NiICl [46]. However, in the case of CrIX, as the spin spiral is primarily driven by the $J_1 - J_2$ frustration, modulation of J_1 by the electric field has a significant impact on the wavelength. Additionally, we validate these two distinct origins of the tuning of the spin-spiral θ and λ by artificially varying the Heisenberg matrix in Fig. S7 [31]. We also confirm that the effect of SIA is negligible in controlling the inclination plane (Fig. S8 [31]). Hence, tuning of θ and λ demonstrates precise magnetoelectric control over the spin spiral.

The maximum field considered here, 0.50 V/Å, should be regarded as an upper-bound theoretical value used to clearly reveal the microscopic trends. Specialized dual ionic-liquid gating has generated perpendicular fields of approximately 4 V/nm in monolayer 2D materials [58], indicating that fields approaching the regime considered here may be experimentally attainable in appropriately designed devices. Nevertheless, the lower-field points in Fig. 7 already exhibit the same continuous trends. We therefore expect the proposed tuning mechanism to persist at experimentally accessible fields, although with correspondingly smaller changes in the magnetic interactions. Experimentally, the associated change in the spin-spiral wavelength could, in principle, be identified from a shift of the magnetic propagation vector measured by neutron scattering, as field-induced changes in the helical pitch have been directly resolved using small-angle neutron scattering [59]. Similarly, changes in the spiral-plane orientation could be resolved using polarized-neutron diffraction, which has been employed to determine the orientation and reorientation of helical spin planes in noncollinear magnets [60].

While our electric field calculations do not reveal a magnetic phase transition within the explored range, the demonstrated sensitivity of the exchange couplings to other external perturbations such as strain or chemical doping points to multiple avenues for further control. A comprehensive exploration of the magnetic phase diagram as a function of these parameters remains an important direction for future research.

IV. SUMMARY

We present a comprehensive first-principles study of Janus CrIBr and CrICl monolayers, focusing on the interplay between frustrated magnetic interactions and structural asymmetry. Our calculations reveal that a JT distortion stabilizes a monoclinic Cm crystal structure, fundamentally dictating the magnetic Hamiltonian including the specific forms of DMI and symmetric anisotropic exchange allowed by the system.

The magnetic ground state is an antiferromagnetic helical spin spiral, primarily driven by intrinsic Heisenberg frustration ($J_1 - J_2$ competition) rather than DMI-induced canting. Through a detailed analysis, we extract the DMI and symmetric anisotropic exchange parameters, alongside SIA. The DMI is enabled by the broken inversion symmetry of the Janus structure, whereas the symmetric anisotropic exchange and SIA reflect the low-symmetry spin-orbit-coupled crystal environment. These significant anisotropic interactions, quantified by substantial $|D/J|$ ratios and comparable symmetric exchange, are crucial in determining and stabilizing the unique tilted spiral plane geometry of the magnetic ground state. These results are confirmed by atomistic spin simulations that predict a Néel temperature $T_N \approx 14.2$ K for CrIBr, in reasonable agreement with experimental reports for the bulk limit.

We demonstrate that the magnetic order is tunable under an external electric field. The inclination plane angle θ is controlled through modulation of anisotropic coupling. Interestingly, the nearest-neighbor isotropic coupling J_1 is more sensitive to electric field perturbation than J_2. This imbalance directly tunes the frustration ratio $|J_2/J_1|$, shifting the spin-spiral wavelength λ without any change in the underlying crystal symmetry. Consequently, the electric field can control not only the inclination plane but also control the spin-spiral wavelength. Thus, both θ and λ are governed by distinct microscopic

mechanisms, providing dual control over the spin-spiral properties.

Our findings highlight that the interplay between Janus asymmetry and JT distortion offers a broadly applicable strategy for engineering magnetic frustration in two-dimensional magnets. This mechanism and analysis should extend to any Janus monolayer derived from a JT-active parent compounds. These results establish Janus Cr$I$$X$ monolayers as a promising platform for exploring frustration-driven chiral magnetism and provide microscopic insight into electric-field manipulation of non-collinear JT-active Janus magnetic spin textures in 2D magnets.

ACKNOWLEDGMENTS

This work was partly supported by MEXT DX-Mag (Grant No.JPMXP1122715503), JSPS KAKENHI (GrantNo. JP24K01144), and the Spintronics Research Network of Japan (Spin-RNJ). The calculations were partly carried out using supercomputers at ISSP, the University of Tokyo, and TSUBAME, Institute of Science Tokyo.

[1] M. M. Vopson, Fundamentals of multiferroic materials and their possible applications, Crit. Rev. Solid State Mater. Sci. **40**, 223 (2015).

[2] T. Lottermoser, T. Lonkai, U. Amann, D. Hohlwein, J. Ihringer, and M. Fiebig, Magnetic phase control by an electric field, Nature **430**, 541 (2004).

[3] T. Taniyama, Electric-field control of magnetism via strain transfer across ferromagnetic/ferroelectric interfaces, J. Phys.: Condens. Matter **27**, 504001 (2015).

[4] Q. Song, C. A. Occhialini, E. Ergeçen, B. Ilyas, D. Amoroso, P. Barone, J. Kapeghian, K. Watanabe, T. Taniguchi, A. S. Botana, S. Picozzi, N. Gedik, and R. Comin, Evidence for a single-layer van der Waals multiferroic, Nature **602**, 601–605 (2022) .

[5] M. Mostovoy, Multiferroics: Different routes to magnetoelectric coupling, npj Spintronics **2**, 18 (2024).

[6] J. A. Schneeloch, S. Liu, P. V. Balachandran, Q. Zhang, and D. Louca, Helimagnetism in the candidate ferroelectric CrI_2, Phys. Rev. B **109**, 144403 (2024).

[7] H.-S. Yu, X.-S. Ni, and K. Cao, Sliding multiferrocity in van der Waals layered CrI_2, npj Comput. Mater. (2025).

[8] H. Y. Widyandaru and Y. Gohda, Tunable magnetic coupling of monolayer CrI_2 by strain engineering, npj Spintronics **3**, 34 (2025).

[9] I. E. Dzyaloshinskii, Thermodynamic theory of weak ferromagnetism in antiferromagnetic substances, Sov. Phys. JETP **5**, 1259 (1957).

[10] T. Moriya, Anisotropic superexchange interaction and weak ferromagnetism, Phys. Rev. **120**, 91 (1960).

[11] K. Acharya, K. Huang, E. Y. Tsymbal, and T. R. Paudel, First-principles investigation of the emergence of multiferroicity and skyrmions in CrI_2, Phys. Rev. B **111**, 094435 (2025).

[12] B. Valdés-Toro, I. Ferreira-Araya, R. Gallardo, and J. W. González, Stacking-controlled magnetic exchange and magnetoelectric coupling in bilayer CrI_2, Nanoscale (2026).

[13] M. Bode, M. Heide, K. Von Bergmann, P. Ferriani, S. Heinze, G. Bihlmayer, A. Kubetzka, O. Pietzsch, S. Blügel, and R. Wiesendanger, Chiral magnetic order at surfaces driven by inversion asymmetry, Nature **447**, 190 (2007).

[14] J. Jiang and W. Mi, Two-dimensional magnetic Janus monolayers and their van der Waals heterostructures: a review on recent progress, Mater. Horiz. **10**, 788 (2023).

[15] R. Li, Y. Cheng, and W. Huang, Recent progress of Janus 2D transition metal chalcogenides: from theory to experiments, Small **14**, 1802091 (2018).

[16] A.-Y. Lu, H. Zhu, J. Xiao, C.-P. Chuu, Y. Han, M.-H. Chiu, C.-C. Cheng, C.-W. Yang, K.-H. Wei, Y. Yang, Y. Wang, D. Sokaras, D. Nordlund, P. Yang, D. A. Muller, M.-Y. Chou, X. Zhang, and L.-J. Li, Janus monolayers of transition metal dichalcogenides, Nat. Nanotechnol. **12**, 744–749 (2017) .

[17] R. Sant, M. Gay, A. Marty, S. Lisi, R. Harrabi, C. Vergnaud, M. T. Dau, X. Weng, J. Coraux, N. Gauthier, O. Renault, G. Renaud, and M. Jamet, Synthesis of epitaxial monolayer Janus SPtSe, npj 2D Mater. Appl. **4**, 41 (2020) .

[18] J. A. Schneeloch, A. A. Aczel, and D. Louca, Helimagnetism in $CrBr_2$ and CrIBr, Phys. Rev. B **111**, 054403 (2025).

[19] Z. Guan, Z. Shen, Y. Xue, T. Zhong, X. Wu, and C. Song, Electronic properties, skyrmions and bimerons in Janus CrXY (X, Y= S, Se, Te, Cl, Br, I, and X$\neq$ Y) monolayers, Phys. Chem. Chem. Phys. **25**, 24968 (2023).

[20] L. Yang, Y. Gao, M. Wu, and P. Jena, Interfacial triferroicity in monolayer chromium dihalide, Phys. Rev. B **105**, 094101 (2022).

[21] L. Peng, J. Zhao, M. Cai, G.-Y. Hua, Z.-Y. Liu, H.-N. Xia, Y. Yuan, W.-H. Zhang, G. Xu, L.-X. Zhao, Z.-W. Zhu, T. Xiang, and Y.-S. Fu, Mott phase in a van der Waals transition-metal halide at single-layer limit, Phys. Rev. Res. **2**, 023264 (2020) .

[22] C. Xu, J. Feng, H. Xiang, and L. Bellaiche, Interplay between Kitaev interaction and single ion anisotropy in ferromagnetic CrI_3 and $CrGeTe_3$ monolayers, npj Comput. Mater. **4**, 57 (2018).

[23] I. Lee, F. G. Utermohlen, D. Weber, K. Hwang, C. Zhang, J. van Tol, J. E. Goldberger, N. Trivedi, and P. C. Hammel, Fundamental spin interactions underlying the magnetic anisotropy in the Kitaev ferromagnet CrI_3, Phys. Rev. Lett. **124**, 017201 (2020) .

[24] N. D. Mermin and H. Wagner, Absence of ferromagnetism or antiferromagnetism in one-or two-dimensional isotropic Heisenberg models, Phys. Rev. Lett. **17**, 1133 (1966).

[25] P. E. Blöchl, Projector augmented-wave method, Phys. Rev. B **50**, 17953 (1994).

[26] J. P. Perdew, K. Burke, and M. Ernzerhof, Generalized

gradient approximation made simple, Phys. Rev. Lett. **77**, 3865 (1996).
[27] G. Kresse and J. Furthmüller, Efficient iterative schemes for ab initio total-energy calculations using a plane-wave basis set, Phys. Rev. B **54**, 11169 (1996).
[28] S. Grimme, J. Antony, S. Ehrlich, and H. Krieg, A consistent and accurate *ab initio* parametrization of density functional dispersion correction DFT-D for the 94 elements H-Pu, J. Chem. Phys. **132**, 154104 (2010).
[29] S. L. Dudarev, G. A. Botton, S. Y. Savrasov, C. J. Humphreys, and A. P. Sutton, Electron-energy-loss spectra and the structural stability of nickel oxide: An LSDA+U study, Phys. Rev. B **57**, 1505 (1998).
[30] M. Cococcioni and S. de Gironcoli, Linear response approach to the calculation of the effective interaction parameters in the LDA+U method, Phys. Rev. B **71**, 035105 (2005).
[31] See Supplemental Material at `http://link.aps.org/supplemental/10.1103/kq2k-5dfg` for "Interplay of Heisenberg frustration and anisotropic exchange in the magnetoelectric coupling of Janus CrIX (X = Cl, Br) monolayers." .
[32] Y. Gohda, Y. Nakamura, K. Watanabe, and S. Watanabe, Self-consistent density functional calculation of field emission currents from metals, Phys. Rev. Lett. **85**, 1750 (2000).
[33] X. Li, H. Yu, F. Lou, J. Feng, M.-H. Whangbo, and H. Xiang, Spin hamiltonians in magnets: theories and computations, Molecules **26**, 803 (2021).
[34] J. G. Rau, E. K.-H. Lee, and H.-Y. Kee, Generic spin model for the honeycomb iridates beyond the Kitaev limit, Phys. Rev. Lett. **112**, 077204 (2014).
[35] J. L. Lado and J. Fernández-Rossier, On the origin of magnetic anisotropy in two dimensional CrI_3, 2D Mater. **4**, 035002 (2017).
[36] D. Šabani, C. Bacaksiz, and M. V. Milošević, *Ab initio* methodology for magnetic exchange parameters: Generic four-state energy mapping onto a Heisenberg spin hamiltonian, Phys. Rev. B **102**, 014457 (2020).
[37] H. J. Xiang, E. J. Kan, S.-H. Wei, M.-H. Whangbo, and X. G. Gong, Predicting the spin-lattice order of frustrated systems from first principles, Phys. Rev. B **84**, 224429 (2011).
[38] H. Xiang, C. Lee, H.-J. Koo, X. Gong, and M.-H. Whangbo, Magnetic properties and energy-mapping analysis, Dalton Trans. **42**, 823 (2013).
[39] R. F. L. Evans, W. J. Fan, P. Chureemart, T. A. Ostler, M. O. A. Ellis, and R. W. Chantrell, Atomistic spin model simulations of magnetic nanomaterials, J. Phys.: Condens. Matter **26**, 103202 (2014).
[40] P. Li, N. Liu, J. Zhang, S. Chen, X. Zhou, D. Guo, C. Wang, W. Ji, and D. Zhong, Two-dimensional magnetic semiconducting heterostructures of single-layer CrI_3–CrI_2, ACS Appl. Mater. Interfaces **15**, 19574 (2023).
[41] F. Liu, T. Huang, L. Hai, Z. Shi, X. Qiu, S. M. Zhou, and W. Fan, Effects of asymmetric Dzyaloshinskii–Moriya interaction on noncollinear antiferromagnetic spin chiral switching, SPIN **15**, 2540002 (2025).
[42] A. Fert, V. Cros, and J. Sampaio, Skyrmions on the track, Nat. Nanotechnol. **8**, 152 (2013).
[43] J. Liang, W. Wang, H. Du, A. Hallal, K. Garcia, M. Chshiev, A. Fert, and H. Yang, Very large Dzyaloshinskii-Moriya interaction in two-dimensional Janus manganese dichalcogenides and its application to realize skyrmion states, Phys. Rev. B **101**, 184401 (2020).
[44] Z. He, W. Du, K. Dou, Y. Dai, B. Huang, and Y. Ma, Ferroelectrically tunable magnetic skyrmions in two-dimensional multiferroics, Mater. Horiz. **10**, 3450 (2023).
[45] Q. Cui, J. Liang, Z. Shao, P. Cui, and H. Yang, Strain-tunable ferromagnetism and chiral spin textures in two-dimensional Janus chromium dichalcogenides, Phys. Rev. B **102**, 094425 (2020).
[46] X. Li, Z. Wang, Z. Chen, Z. Yu, and C. Xu, Dzyaloshinskii-Moriya interaction manipulation in multiferroic Janus monolayers, npj Comput. Mater. **11**, 123 (2025).
[47] R. Caglayan, A. Mogulkoc, Y. Mogulkoc, M. Modarresi, and A. Rudenko, Dzyaloshinskii-Moriya interaction and nontrivial spin textures in the Janus semiconductor monolayers VXY (X= Cl, Br, I; Y= S, Se, Te), Phys. Rev. B **110**, 094440 (2024).
[48] C. Jiang, K. Lu, R. Wang, Q. Chen, and J. Wang, Magnetic anisotropy and Jahn-Teller effect in ferromagnetic two-dimensional $CrGa_2Te_4$, ACS Appl. Electron. Mater. **4**, 3220 (2022).
[49] Y. O. Kvashnin, A. Bergman, A. I. Lichtenstein, and M. I. Katsnelson, Relativistic exchange interactions in CrX_3 (X = Cl, Br, I) monolayers, Phys. Rev. B **102**, 115162 (2020).
[50] L. Li, B. Zhang, Z. Chen, C. Xu, and H. Xiang, Effects of kitaev interaction on magnetic order and anisotropy, Phys. Rev. B **110**, 214435 (2024).
[51] C. Kim, O. Vilella, Y. Lee, *et al.*, Kitaev interaction and proximate higher-order skyrmion crystal in the triangular lattice van der Waals antiferromagnet NiI_2, npj Quantum Mater. (2026).
[52] M. Heide, G. Bihlmayer, and S. Blügel, Dzyaloshinskii-moriya interaction accounting for the orientation of magnetic domains in ultrathin films: Fe/W (110), Phys. Rev. B **78**, 140403 (2008).
[53] A. A. Katanin and V. Y. Irkhin, Magnetic order and spin fluctuations in low-dimensional insulating systems, Phys.-Usp. **50**, 613 (2007).
[54] R. F. L. Evans, U. Atxitia, and R. W. Chantrell, Quantitative simulation of temperature-dependent magnetization dynamics and equilibrium properties of elemental ferromagnets, Phys. Rev. B **91**, 144425 (2015).
[55] C. Dupas and J.-P. Renard, Effect of impurities on the Néel temperature and the low-temperature magnetic susceptibility of the quasi-one-dimensional antiferromagnet TMMC, Phys. Rev. B **18**, 401 (1978).
[56] T. P. T. Nguyen, K. Yamauchi, T. Oguchi, D. Amoroso, and S. Picozzi, Electric-field tuning of the magnetic properties of bilayer VI_3: A first-principles study, Phys. Rev. B **104**, 014414 (2021).
[57] F. Heully-Alary, B. Pradines, N. Suaud, and N. Guihéry, Physical origin of the anisotropic exchange tensor close to the first-order spin–orbit coupling regime and impact of the electric field on its magnitude, J. Chem. Phys. **161**, 054310 (2024).
[58] B. I. Weintrub, Y.-L. Hsieh, S. Kovalchuk, J. N. Kirchhof, K. Greben, and K. I. Bolotin, Generating intense electric fields in 2d materials by dual ionic gating, Nat. Commun. **13**, 6601 (2022).
[59] N. Kanazawa, J. S. White, H. M. Rønnow, C. D. Dewhurst, Y. Fujishiro, A. Tsukazaki, Y. Kozuka, M. Kawasaki, M. Ichikawa, F. Kagawa, and Y. Tokura,

Direct observation of anisotropic magnetic field response of the spin helix in FeGe thin films, Phys. Rev. B **94**, 184432 (2016) .
[60] S. Grigoriev, S. Maleyev, A. Okorokov, Y. O. Chetverikov, P. Böni, R. Georgii, D. Lamago, H. Eckerlebe, and K. Pranzas, Magnetic structure of mnsi under an applied field probed by polarized small-angle neutron scattering, Phys. Rev. B **74**, 214414 (2006).